IEEE Transactions on Nuclear Science, Vol.NS-22, February 1975

A COMPARATIVE STUDY OF 3-D IMAGE RECONSTRUCTION ALGORITHMS WITH REFERENCE TO NUMBER OF PROJECTIONS AND NOISE FILTERING *,**

by

Z. H. Cho,* J. K. Chan *

Lab. of Nuc. Med. & Rad. Biology, Electrical Sci. & Engr. Dept.
University of California, Los Angeles

E. L. Hall,** R. P. Kruger,** D. G. McCaughey **

Image Processing Institute, Electrical Engr. Dept.
University of Southern California
Los Angeles, California

ABSTRACT

A comparative study of four popular 3-D image reconstruction algorithms has been made. Particular attention was given to artifacts generated and noise sensitivity. The methods considered include two spatial domain convolution algorithms, the Linear Superposition with Compensation (LSC) and a Fourier Convolution Method (FCM), a direct Fast Fourier Transform method (FFT), and an algebraic technique, the Simultaneous Iterative Reconstruction Technique (SIRT). The methods were compared by computing reconstructed images for an identical input phantom image. The phantom image contains several edges and a 2% contrast object. Variations, artifacts and noise sensitivity are easily visualized by perspective plots of the reconstructed images. Considerations as to the optimum algorithm for a particular application are discussed.

I. INTRODUCTION

Recent 3-D image reconstruction techniques [1] have wide application in nuclear science since they provide a method for viewing the interior secions of an object without physically destroying the object. The widespread use of these methods especially in nuclear medicine and radiology have raised many exciting questions concerning artifact generation, minimum required number of projections, effects of noise statistics, filtering methods and computation speed. With a number of given constraints, such as finite exposure time, the effect of energy averaging (from a polyenergetic source either of Bremsstrahlung x-rays or from a multiple peak, radioactive source), projection geometry, and inherent precision (such as the positron camera case), it is possible to choose an optimum computing algorithm. An important application of 3-D image reconstruction has been transverse axial transmission tomography using x-rays. This method requires statistics of better than 0.5% in determination of the linear attenuation coefficient and also requires a large number of points for each projection as well as a large number of projections. Another important application where 3-D image reconstruction algorithms can be applied is in tomography systems for positron emitting isotopes which utilize coincidence detection of annihilation gamma rays to obtain the image reconstruction information [3, 4].

Computer implementation of 3-D image reconstruction may be accomplished in several ways. Three of these are linear superposition, Fourier transform, and algebraic. The advantages of each techniques appear to be application dependent and a general theoretical comparison is difficult. In this paper a theoretical development and experimental comparison will be made of the following techniques:

a) Linear Superposition with Compensation (LSC) [5, 6, 7]

b) Fourier Convolution Technique (FCT) [8, 9, 10]

c) Fast Fourier Transform (FFT) [11]

d) Simultaneous Iterative Reconstruction Technique (SIRT) [13, 14, 15].

A comparison of the above methods will be made on the basis of image quality with a given number of projections and given statistics.

The basic nature and essential part of 3-D image reconstruction seems to be the actual scanning or data collection mechanism which is known (mostly in the medical field) as "Transverse Axial Scanning". It is therefore often called Transverse Axial Tomography (TAT), or more specifically, Computerized Transverse Axial Tomography (CTAT). Although there exist few alternative scanning or data collection methods, we shall, in this paper, be confined to the Transverse Axial Scanning mode (fan beam geometry is a variation of parallel beam). In this mode, a first order image reconstruction can be obtained by simple linear superposition (which is also known as back projection). In a more complex situation, however, the image reconstruction is grossly deviated by the blurring, particularly the central portion of the image, due to the nature of the axial scanning mode.

To introduce the methods suppose that the Fourier transform of $f(x, y)$ is $F(f_x, f_y)$. The general expression is a simple well-known two dimensional Fourier transform, as illustrated in Fig. 1, i.e.,

*This work was supported by U.S. Atomic Energy Commission under contract AT(04-1) GEN-12.

**This work was partially supported by the Advanced Research Projects Agency of the Department of Defense and was monitored by the Air Force Eastern Test Range under Contract No. F08606-72-C-0008, ARPA Order No. 1706 and also by NIH Training Grant GM 01724.

$$f(x,y) = \int_{-\infty}^{\infty}\int_{-\infty}^{\infty} F(f_x, f_y)\exp[2\pi i(f_x X + f_y Y)]df_x df_y \quad (1)$$

By virtue of the circularly symmetrical nature of CTAT concepts, Eq. (1) can be transformed into polar coordinates, i.e.,

$$f(r,\emptyset) = \int_0^{\pi}\int_{-\infty}^{\infty} F(R,\psi)|R|\exp[2\pi i R\ r\cos(\psi-\emptyset)]dRd\psi \quad (2)$$

where $|R|$ is the ramp function in the Fourier domain arising from the coordinate transformation, and x, y, f_x, f_y, ψ, and $\emptyset$ have the following relationships:

$$x = r\cos\emptyset,\ y = r\sin\emptyset,\ \emptyset = \tan^{-1} y/x$$

$$f_x = R\cos\psi,\ f_y = R\sin\psi,\ \psi = \tan^{-1} f_y/f_x$$

$$\psi = \theta + \pi/2$$

Eq. (2) can then also be denoted as

$$f(r,\emptyset) = \int_0^{\pi}\int_{-\infty}^{\infty} F(R,\theta)|R|\exp[2\pi i R\ r\sin(\theta-\emptyset)]dRd\theta \quad (3)$$

where $F(R;\theta) = F[f(\ell;\theta)] = \int_{-\infty}^{\infty} f(\ell;\theta)\exp[-2\pi i R\ell]d\ell$

$F(R;\theta)$ therefore represents the Fourier transform of the projection $f(\ell;\theta)$.

If, however, one makes a simple Fourier transform with $F(R;\theta)$, it results in the linear superposition reconstruction image $f_{LS}(r,\emptyset)$, i.e.,

$$f_{LS}(r,\emptyset) = \int_0^{\pi}\int_{-\infty}^{\infty} F(R,\theta)\exp[2\pi i R r\sin(\theta-\emptyset)]dRd\theta \quad (4)$$

This is in effect the same as

$$f_{LS}(r,\emptyset) = \int_0^{\pi}\int_{-\infty}^{\infty} F(R,\theta)|R||R|^{-1}\exp[2\pi R r\sin(\theta-\emptyset)]dRd\theta$$

$$= f(r,\emptyset) * \frac{1}{r} \quad (5)$$

The correct image $f(r,\emptyset)$ can therefore be obtained by deconvolving the $1/r$ function, i.e.,

$$f(r,\emptyset) = f_{LS}(r,\emptyset) * r = \int_0^{\pi}[f(\ell,\theta) * \varphi(\ell)]d\theta \quad (6)$$

Now the deconvolution function $\varphi(\ell)$ is

$$\varphi(\ell) = \int_{-R_1}^{R_1} |R|\exp[2\pi i R\ \ell]dR. \quad (7)$$

Eqs. (1) through (7) cover the basic nature of the image blurring and deblurring principles. Eqs. (2) and (3), for example, suggest a direct Fourier transform to obtain the reconstructed and deblurred images in the spatial domain, while eqs. (5) and (6) indicate a direct convolution or deconvolution process in the spatial domain, as will be detailed in the following.

Another method suggested in the earlier stage of the 3-D image reconstruction era is the Iterative method, more widely known as the Algebraic Reconstruction Technique (ART) [13], and its family [14,15]. This ART method and its modified version known as SIRT will be detailed in a separate section.

2. RECONSTRUCTION ALGORITHMS

Spatial domain deconvolution methods.

If we focus our attention on a possible spatial domain processing method, a proper deconvolution function $\varphi(\ell)$ can be found. This process is equivalent to searching for a suitable low pass filter function. Four deconvolution functions which are considered to be representative will be described in the following.

a. Linear Superposition with Compensation and its deblurring function.

The simplest technique known for years in nuclear medicine and diagnostic radiology is the linear superposition technique [16]. However, to obtain a correctly reconstructed image, the proper deblurring function is required. A deblurring function known as the Transfer Function (LSC) was proposed by Cho et. al. and results in the technique called Linear Superposition with Compensation (LSC). In this case, the deblurring function, $\varphi(\ell)$, is derived in the spatial domain (detailed derivation is described in refs. [5], [6], and [7]). The LSC deblurring function (Fig. 3(a)) is the spatial domain equivalent of the $F^{-1}[|R|]$, given in eq. (8) and can be expressed as (see also Fig. 2 and 3),

$$\varphi(\ell) = f(na) = 1 \qquad ; n = 0$$

$$\varphi(\ell) = f(na) = I_{c_1} = -I_{r1} = -\frac{A_1}{A'_1} \qquad ; n = 1$$

$$\varphi(\ell) = f(na) = I_{c_n} \quad (8)$$

$$= \frac{2(I_{r1}A'_n + I_{r2}A''_n + \cdots + I_{r,n-1}A_n^{n-1}) - A_n}{A_n^n}$$

$$= \frac{2\sum_{i=1}^{n-1} I_{ri}A_n^i - A_n}{A_n^n} \qquad ; n = \pm 2, \pm 3$$

The use of the deblurring function (transfer function) given in eq. (8) and linear superposition using weighting factors W_{ij} is detailed in refs. [5], [6], and [7].

b. The Fourier-Convolution Technique and its deconvolution function [8, 9].

According to Shepp and Logan [8], and Ramachandran

and Lakshiminarayan [9], the deconvolution function derived from Fourier domain (frequency domain) can be written in a discrete form as

$$\varphi(\ell)[\Rightarrow f(r)] = f(na) = \frac{4}{\pi a^2} \quad ; n = 0$$

$$\varphi(\ell) = f(na) = \frac{-4}{\pi a^2(4K^2-1)} \quad ; k = \pm 1, \pm 2, \ldots \tag{9}$$

and is shown in Fig. 3(b).

c. $F^{-1}[|R|]$ Function and other simple spatial domain deblurring functions.

According to Bracewell [10], the Fourier transform of the $|R|$ in finite bandwidth, i.e., $\pm R_1$, leads to

$$\int_{-R_1}^{R_1} |R| \exp[2\pi R.\, r]dR = \int_{-R_1}^{R_1} \left\{ \mathrm{rect}\left[\frac{R}{2R_1}\right] - \Lambda\left[\frac{R}{R_1}\right] \right\} \cdot \exp[2\pi i R.\, r]dR \tag{10}$$

where $\mathrm{rect}\left[\frac{R}{2R_1}\right]$ and $\Lambda\left[\frac{R}{R_1}\right]$ corresponds to rectangular and triangular functions, respectively.

The result is then

$$\varphi(\ell)[\Rightarrow f(r)] = 2R_1 \,\mathrm{sinc}(2R_1 r) - R_1 \,\mathrm{sinc}^2(R_1 r) \tag{11}$$

where $r = na$ with n an integer.

This deblurring function is also shown in Fig. 3 as an analog form (Fig. 3(c)).

d. A simpler form similar to the eqs. (10) and (11) is the simple sinc function. The reason that the simple sinc function works at all is due to the fact that the sinc function in spatial domain corresponds to the bandwidth limited function in the frequency domain.

Fourier transform methods.

The Fourier transform method is perhaps the most convenient and basic form of 3-D image reconsturction method, and has been proposed by several investigators [10] and [11]. Although there are many methods for reconstruction using the Fourier and other transforms, two illustrative methods will be considered. One involves frequency domain interpolation while the other uses spatial domain interpolation.

It is easily shown for both the continuous and discrete cases that the Fourier transform of a projection at 0° equals the central section of the transform of the object. However, the discrete transform of the projection at oblique angles equals the transform sampled at oblique angles. Thus the discrete transform points are produced on a polar grid rather than a rectangular grid. Since the fast Fourier transform algorithm requires a rectangular grid, an interpolation is required. The interpolation is further complicated by the complex nature of the Fourier transform. Although the magnitude of these complex numbers are highly correlated, the phase terms are independent. Particular difficulty is produced if consecutive points have opposite signs, i.e., $(2n+1)\pi$ phase shifts. One partial solution to this problem is to transform the Fourier transform points to minimize the phase variation, perform the interpolation, then perform the inverse of Fourier transformation. The main advantage of frequency domain interpolation is the simplicity and efficiency of the fast Fourier transform algorithm.

The second method uses a Bessel function expansion to permit a polar coordinate Fourier transform computation. This produces an image known on a discrete polar grid in the spatial domain. Spatial domain interpolation is then used to obtain a final image.

Let $F(R, \theta)$ denote the Fourier transform of the projection at angle θ and $f(r, \emptyset)$ be the tomographic section in polar coordinates, and the exact reconstruction is given by

$$f(r, \emptyset) = \int_0^{2\pi}\int_0^{\infty} F(R, \theta)\exp[2\pi j r R \cos(\theta - \emptyset)] R dR d\theta \tag{12}$$

where ψ is now simply denoted as θ for convenience. The transform values are known only at discrete angles, θ_k and radii, R_ℓ. Thus the numerical integration must be used to obtain an estimate $f(r, \emptyset)$, of the image.

$$f(r, \emptyset) = \sum_{\theta_k} \sum_{R_\ell} F(R_\ell, \theta_k)\exp(2\pi j r R_\ell \cos(\theta_k - \emptyset)) R_\ell \Delta R \Delta\theta \tag{13}$$

This computation may be interpreted as a discrete polar coordinate Fourier transform if discrete values of r_m and θ_n are sufficient.

Since the frequency domain interpolation could introduce spurious edges in the image, it would seem desirable to employ an algorithm that utilizes the Fourier coefficients directly on polar coordinates. Crowther, De Rosier and Klug proposed such an algorithm using the Fourier-Bessel transform [11]. Crowther et. al. have employed this algorithm in the reconstruction of images obtained in electron microscopy with reasonable results.

On the polar coordinate transform, note that

a) $\cos(\theta - \emptyset) = \sin(\theta - \emptyset + \pi/2)$.

b) $\exp(ja \sin x) = \sum_{k=-\infty}^{\infty} J_k(a) \exp\{jkx\}$

where $J_k(a)$ is the kth order Bessel function of the first kind. Inserting these two relationships into (12) and rearranging the order of summation and integration, one obtains,

$$f(r, \emptyset) = \sum_{k=-\infty}^{\infty} j^k \int_0^{2\pi}\int_0^{\infty} F(R, \theta) J_k(2\pi r R)\exp\{jk\theta - jk\emptyset\} R dR d\theta$$

where $j^k = \exp[jk\frac{\pi}{2}]$. (14)

If we define

$$f_k(r) = j^k \int_0^{2\pi} \int_0^{\infty} F(R,\theta) J_k(2\pi R r) \exp[jk\theta] R dR d\theta \tag{15}$$

we obtain the Fourier series expression

$$f(r,\emptyset) = \sum_{k=-\infty}^{\infty} f_k(r) \exp\{-jk\emptyset\} \tag{16}$$

Note that (16) is indeed a Fourier series for

$$f_k(r) = \frac{1}{2\pi} \int_0^{2\pi} f(r,\emptyset) \exp\{jk\emptyset\} d\emptyset \tag{17}$$

If we restrict ourselves to discrete angles evenly spaced over $(0, 2\pi)$, (16) becomes a discrete inverse Fourier transform. Knowledge of $f_k(r)$ will permit an exact reconstruction of $f(r,\emptyset)$ along radii equally spaced over $(0, 2\pi)$. $F(R,\theta)$ is in general not available for all R and θ since projections are available for only a discrete set of angles and because a DFT on each projection produces the transform only at discrete frequencies. Therefore, $F_s(R,\theta)$ is the 2-D sampled form of the Fourier transform $F(R,\theta)$ given by

$$F_s(R,\theta) = \frac{2\pi\Delta R}{N} \sum_{i=0}^{I-1} \sum_{n=0}^{N-1} F(i\Delta R, \frac{2\pi n}{N}) \delta(R - i\Delta R, \theta - \frac{2\pi n}{N}) \tag{18}$$

where N = number of projections and I = number of points in each projection.

Inserting (18) into (15) obtains an estimate of $f_k(r)$ termed $\hat{f}_k(r)$ in the form of a Riemann sum

$$\hat{f}_k(r) = \frac{2\pi\Delta R}{N} \sum_{i=0}^{I-1} \sum_{n=0}^{N-1} F(R_i, \frac{2\pi n}{N}) j^k J_k(2\pi R_i r) \cdot R_i \exp\{jk2\pi n/N\} \tag{19}$$

where ΔR has been replaced by R_i. The estimated reconstruction $f(r,\emptyset)$ is then

$$\hat{f}(r,\emptyset) = \sum_{k=-\infty}^{\infty} \hat{f}_k(r) \exp\{-jk\emptyset\} \tag{20}$$

Since $f(r,\emptyset)$ is a space bounded continuous function, $F(R,\theta)$ is an analytic function and thus equation (19) always exists. Equation (19) is in reality retangular integration, and if ΔR and $2\pi/N$ are small, $\hat{f}_k(r)$ is an accurate estimate of $f_k(r)$. The ability to estimate the tomographic section of $f(r,\emptyset)$ with $\hat{f}(r,\emptyset)$ is thus limited only in the accuracy of the $\hat{f}_k(r)$. It can easily be shown that equation (20) can be expressed as

$$\hat{f}(r,\emptyset) = 2\mathrm{Re}\Big[\sum_{k=0}^{\infty} \frac{2\pi\Delta R}{\epsilon_k N} \sum_{i=0}^{I-1} \sum_{n=0}^{N-1} F(R_i, \frac{2\pi n}{N}) J_k(2\pi R_i r) R_i \exp\{jk2\pi n/N - jk(\emptyset - \pi/2)\}\Big] \tag{21}$$

where $\epsilon_k = 2$ for $k=0$ and $\epsilon_k = 1$ for $k \neq 0$, and j^k is again replaced by $\exp\{jk\pi/2\}$. Equation (21) can be computed by a fast Fourier transform operation, followed by a Bessel function weighting operation and a final fast Fourier transform operation.

Algebraic or Iterative Reconstruction Techniques

In the area of 3-D image reconstruction, along with Fourier and convolution techniques an iterative algebraic method (known as ART) [13] has been proposed by Gordon et. al. and a refined version, known as Simultaneous Iterative Reconstruction Technique (SIRT) [14]. For simplicity, we have adopted the latest version employed by Budinger and Gullberg [15], with some modification in the weighting process [5, 6, 7]. The present version probably could be called a Weighted Simultaneous Iterative Reconstruction Technique (WSIRT).

The simultaneous iterative reconstruction method belongs to a class of algebraic reconstruction techniques which are implemented in spatial domain. It was developed by Gilbert [14] and is so called because at each iteration, the densities are changed by using data from all the projections simultaneously, in contrast to ART, where densities are altered using one projection data at a time. The additive SIRT algorithm is

$$\mu^{n+1}(i,j) = \max\{\mu^n(i,j) + \frac{\sum_\theta P_{k(\theta)} \sum_\theta R^n_{k(\theta)}}{\sum_\theta L_{k(\theta)} \sum_\theta N_{k(\theta)}}, 0\} \tag{22}$$

where $\mu(i,j)^n$ and $\mu(i,j)^{n+1}$ are the densities (or attenuation coefficients) evaluated at n^{th} and $(n+1)_{th}$ iterations, respectively, (i,j) represent the pixel which is an element of ray $k(\theta)$; $L_{k(\theta)}$ is the length of the ray $k(\theta)$; $P_{k(\theta)}$ is the measured projected density of the ray $k(\theta)$; $R^n_k(\theta)$ is the projected density of ray $k(\theta)$ after iteration n and $N_{k(\theta)}$ is the number of points in ray $k(\theta)$.

After each iteration, the densities $\mu(i,j)$ are scaled so that their sum over the total array is equal to the sum of one projection data. One particular drawback of this method is the calculation of $R_{k(\theta)}$. $R_{k(\theta)}$ is the sum of the densities associated with the points contained within that ray. The use of $L_{k(\theta)}$ and $N_{k(\theta)}$ is also resulted from this approximation.

For our implementation of SIRT, we used the

weighting factor approach of calculating $R_{k(\theta)}$. Due to this modification, there is no need to use $L_{k(\theta)}$. The modified additive SIRT becomes

$$\mu^{n+1}(i,j) = \max\{\mu^n(i,j) + \frac{\sum_\theta P_{k(\theta)} - \sum R^n_{k(\theta)}}{\sum_\theta A_{k(\theta)}}, 0\} \quad (23)$$

where $A_{k(\theta)}$ is the area of the array crossed by the ray $k(\theta)$. We also stored the $\sum_\theta P_{k(\theta)}$ and $\sum_\theta A_{k(\theta)}$ as the function of the grid points (i, j) so that they can be used for all subsequent iterations.

The advantage of this weighted form of additive SIRT is that it is more accurate and converges faster. From the experimental result so far, there is no sign of divergence as the process goes on.

3. Experimental and Simulation Results.

Three categories of the 3-D image reconstruction algorithms have been simulated using a phantom. Since the question of whether the non-symmetrical object has any significant deviation from the symmetrical one has been proved, for the sake of simplicity and computation cost, only symmetrical phantoms have been used for simulation.

The Figs. (4) through (7) show gradual improvement of the LSC method by increase of correction terms, i.e., for 120 x 120 pattern matrix, the full compensation term would simply be ± 120. In Figs. (8) and (9), image quality as a function of number of projections are shown. In Figs. (10) and (11), the noise dependent image quality are shown.

In Fig. (12), the Fourier-Convolution technique using the deblurring function derived by Shepp and Logan is illustrated. It also shows a well-reconstructed image comparable to the LSC. In Fig. (13), noise immunity of the convolution technique is shown.

In Fig. (14), the results of Fourier transform reconstruction are shown. The image shown in Fig. (14a) was obtained using frequency domain interpolation with linear interpolation between polar and rectangular points. The deviations are due to the inherent interpolation. In Fig. (14b) the results of the Fourier Bessel reconstruction is shown.

In Fig. (17), a vertical section of a monkey head scanned with a nuclear source Gd^{153} is shown. The image reconstruction was done by use of the LSC algorithm. The right side of the figure is the perspective view of the reconstructed image shown in the left.

CONCLUSIONS

At this point in time, it appears that the basic nature of 3-D reconstruction is well understood through the concepts of linear spatial superposition and Fourier transform. In the present comparative study it is concluded that the iterative type algorithms do not appear attractive in reconstruction of 3-D transverse axial images. In general, spatial domain image reconstruction (either LSC or Fourier-Convolution) techniques would appear to be the more efficient and accurate. The Fourier transform method, will probably be faster in reconstructing a large image matrix. For latter, more study and careful programming implementation would seem to be required to obtain comparable image quality with the spatial domain methods.

ACKNOWLEDGEMENT

This work was supported by the USAEC. The authors are grateful to Drs. G. C. Huth and G. Wilson for their enthusiastic support and to Mr. R. Wallis for developing the perspective plot program.

REFERENCES

1. Special Issue on 3-D Image Reconstruction, IEEE on Nucl. Sci., NS-21, No. 3. (1974).

2. EMI 1973 Brochure on Brain Scanner and paper by G. N. Hounsfield (1972). A method of and apparatus for examination of a body by radiation such as x or gamma radiation. The Patent Office, London, Patent Specification 1283915.

3. G. L. Brownell, C. A. Burnham, S. Wilensky, S. Aronow, H. Kazemi, and D. Stieder, in IAEA Medical Isotope Scintigrophy, Vol. HD9697 (1968) 163.

4. M. M. Ter Pogossian, et. al., To be published in J. Of Nuc. Med.

5. Z. H. Cho, I. Ahn, C. Bohm, G. C. Huth, in Physics in Medicine and Biology, Vol. 19, No. 4 (1974) 511.

6. Z. H. Cho, I. Ahn, C. Tsai, in IEEE Nucl. Sci. NS-21, No. 1 (1974) 218.

7. Z. H. Cho, I. Ahn, in Computers in Biomedical Research, Vol. 7, No. 6 (1974).

8. L. A. Shepp and L. Logan, in IEEE Trans. on Nucl. Sci., Special Issue on 3-D Image Reconstruction, NS-21, No. 3, June (1974) 21.

9. G. N. Ramachandran and A. V. Lakshminiarayan, in Proc. of National Acad. of Sciences, USA, Vol. 68, No. 9 (1971) 2236.

10. R. N. Bracewell and A. C. Riddle, "The Inversion of Fan-Beam Scans in Radioastronomy," Astrophysical J., Vol. 150, (1967), pp. 427-434.

11. R. A. Crowther, D. J. DeRosier, and A. Klug, "The Reconstruction of a Three-Dimensional Structure from Projections and its Application to Electron Microscopy," Proc. Loy. Soc. London

A., Vol. 317 (1970), 319-340.

12. R. M. Mersereau, A. V. Oppenheim, in Proc. IEEE, Vol. 62, No. 10, October (1974) 1319.

13. R. Gordon, R. Bender, and G. T. Herman (1970), "Algebraic reconstruction techniques (ART) for three-dimensional electron microscopy and x-ray photography," J. Theor. Biol., Vol. 29, 471-481.

14. P. F. C. Gilbert, J. of Theo. Biology, 36, (1972) 105.

15. T. F. Budinger, G. Gullberg, in IEEE Trans. on Nucl. Sci., NS-21, No. 3 (1974) 1.

16. R. I. Fare, A. C. H. Scott, R. Ollenrenshaw, and G. J. H. Everad, Transverse Axial Tomography, Blackwell Scientific Publications, Oxford, (1964).

17. Z. H. Cho. in Proc. of the 18th Annual Calif. Tech. Meeting of SPIE, Aug. 23, (1974), San Diego, Ca.

18. D. J. DeRosier and A. Klug, in Nature, Vol. 217 (1968) 130.

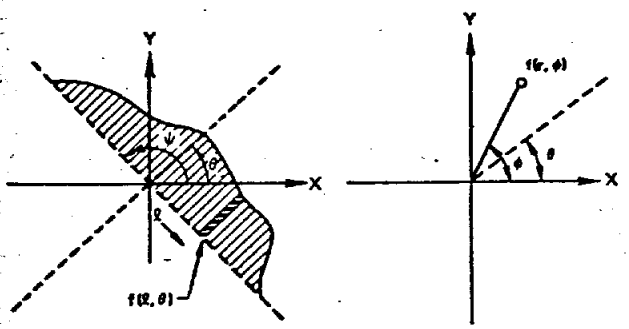

Fig. 1. Coordinates relations in transverse axial scanning. $f(\ell;\theta)$ represents a set of scanning at a given angle, θ.

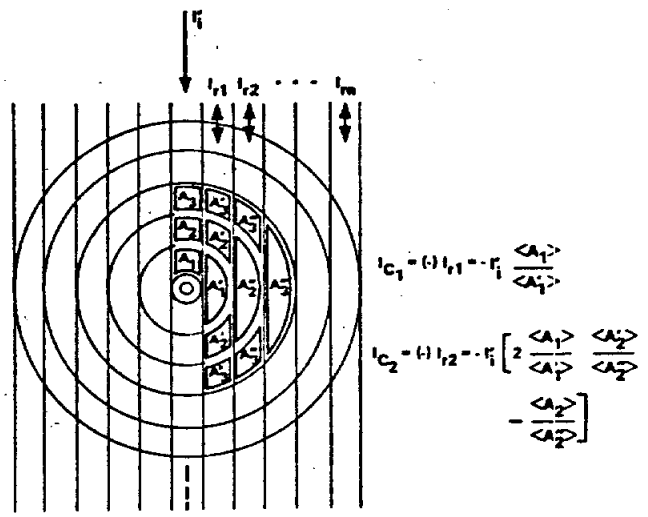

Fig. 2. Derivation procedure for the deblurring function (transfer function in LSC) from 1/r blurring in transverse axial scanning.

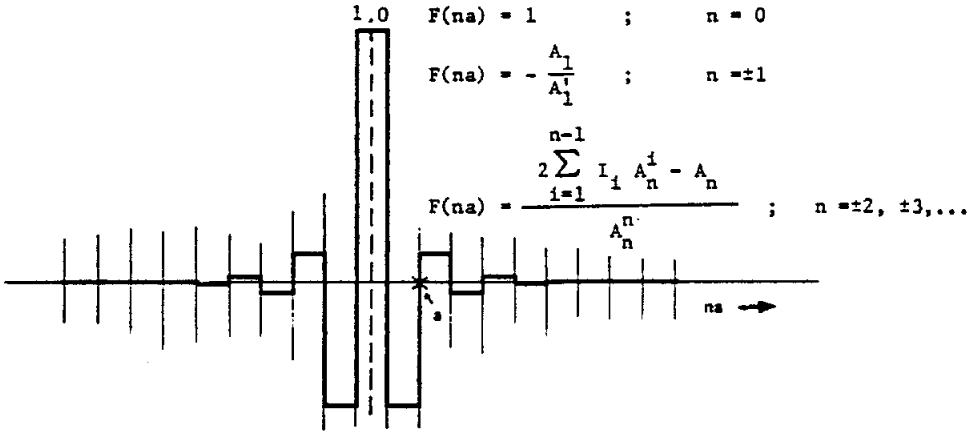

(a) According to LSC Transfer Function (Deblurring Function)

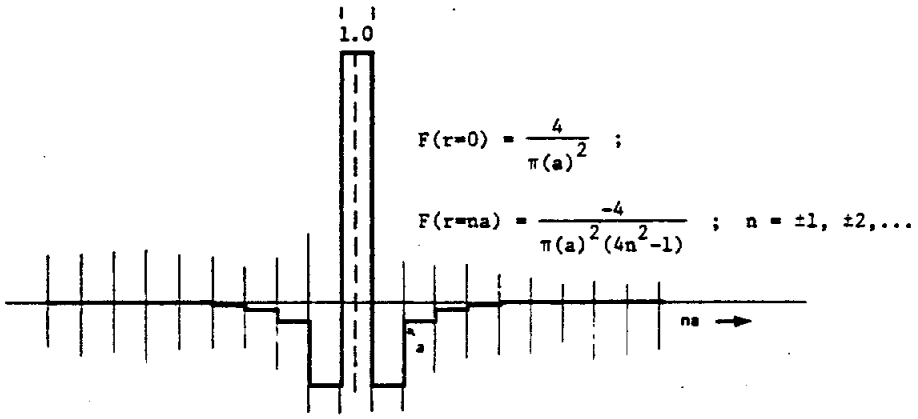

(b) Fourier-Convolution Deblurring Function (According to Shepps & Logan, and Ramachandran & Lakshiminarayan)

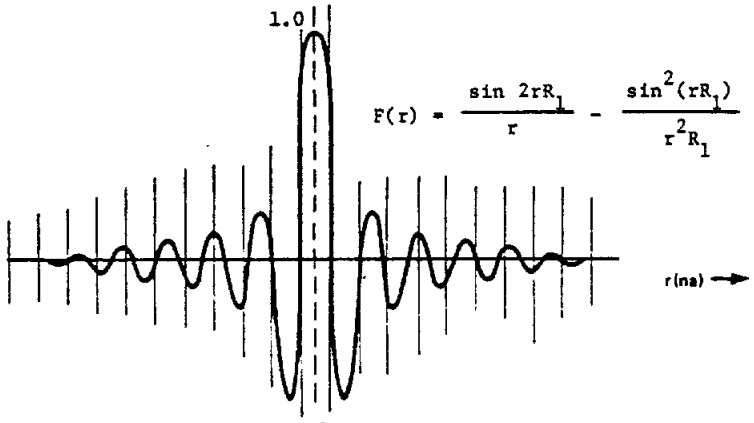

(c) $F^{-1}(|R|)$ Deblurring Function (According to Bracewell & Riddle)

Fig. 3. Variety of deblurring function $\emptyset(\ell)$. The (a) is the deblurring function derived from spatial domain while (b) and (c) are the ones derived from frequency domain.

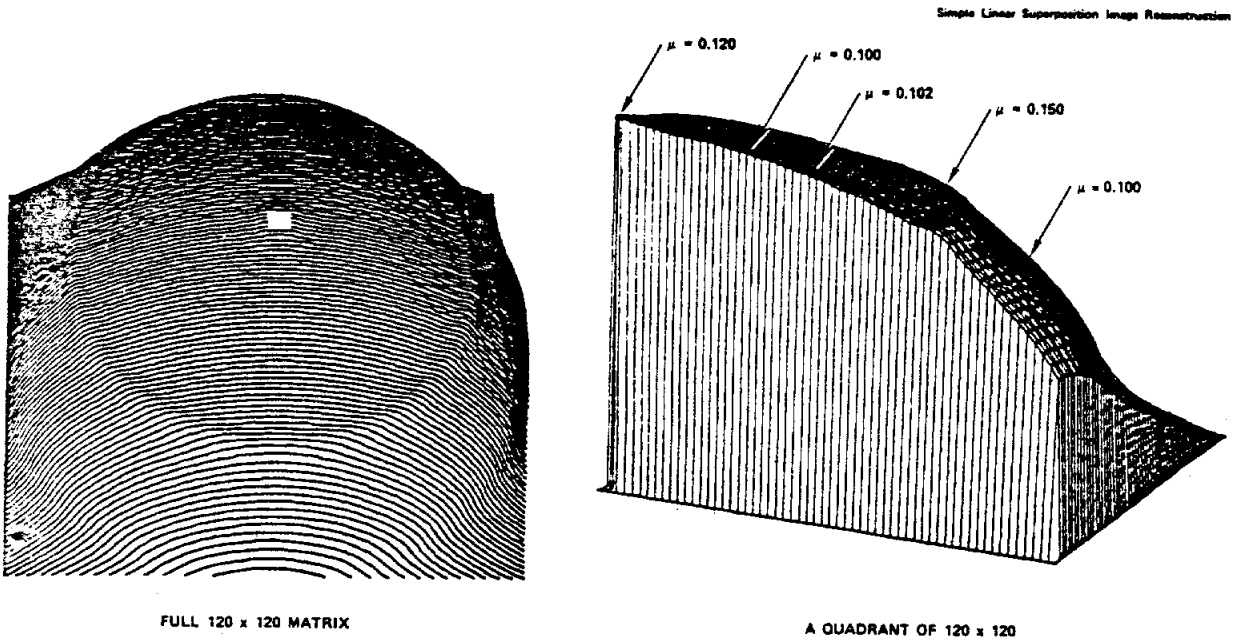

Fig. 4. A reconstruction of a phantom (see Fig. 7) with simple linear superposition.

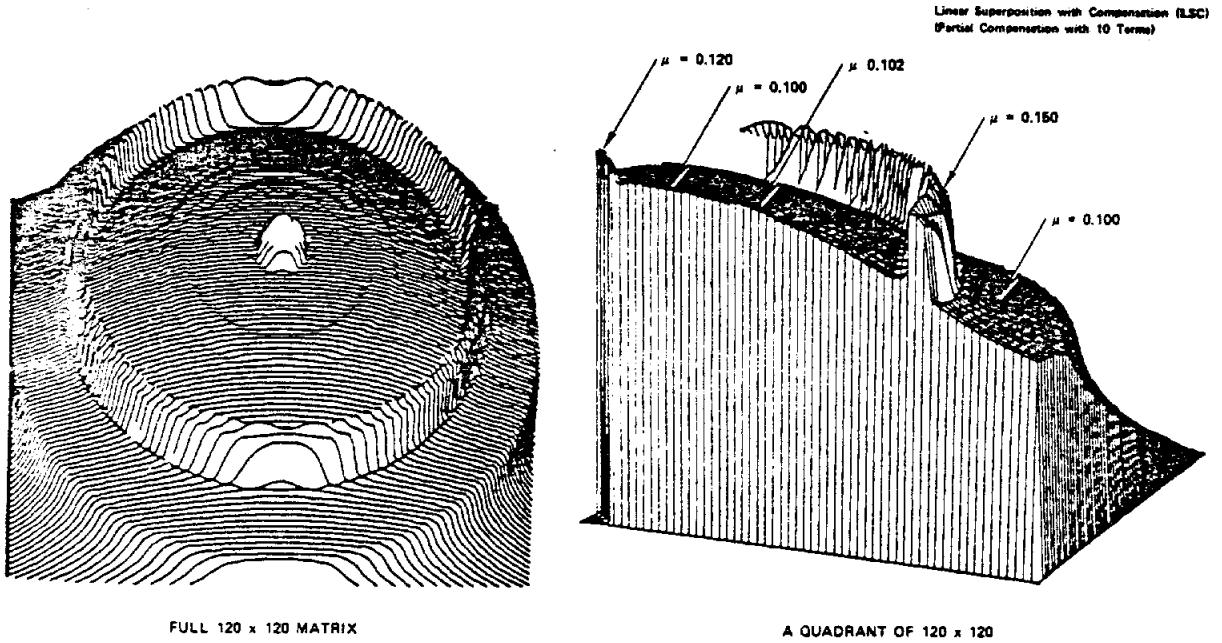

Figure 5.

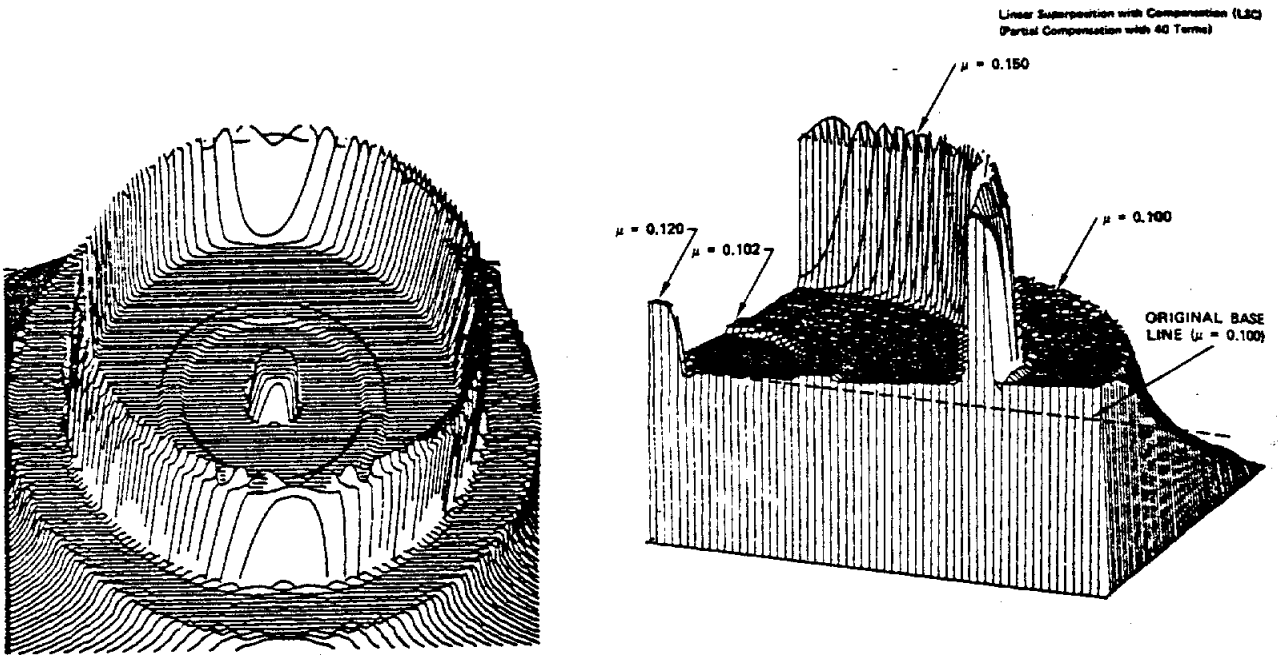

FULL 120 x 120 MATRIX

A QUADRANT OF 120 x 120

Figure 6.

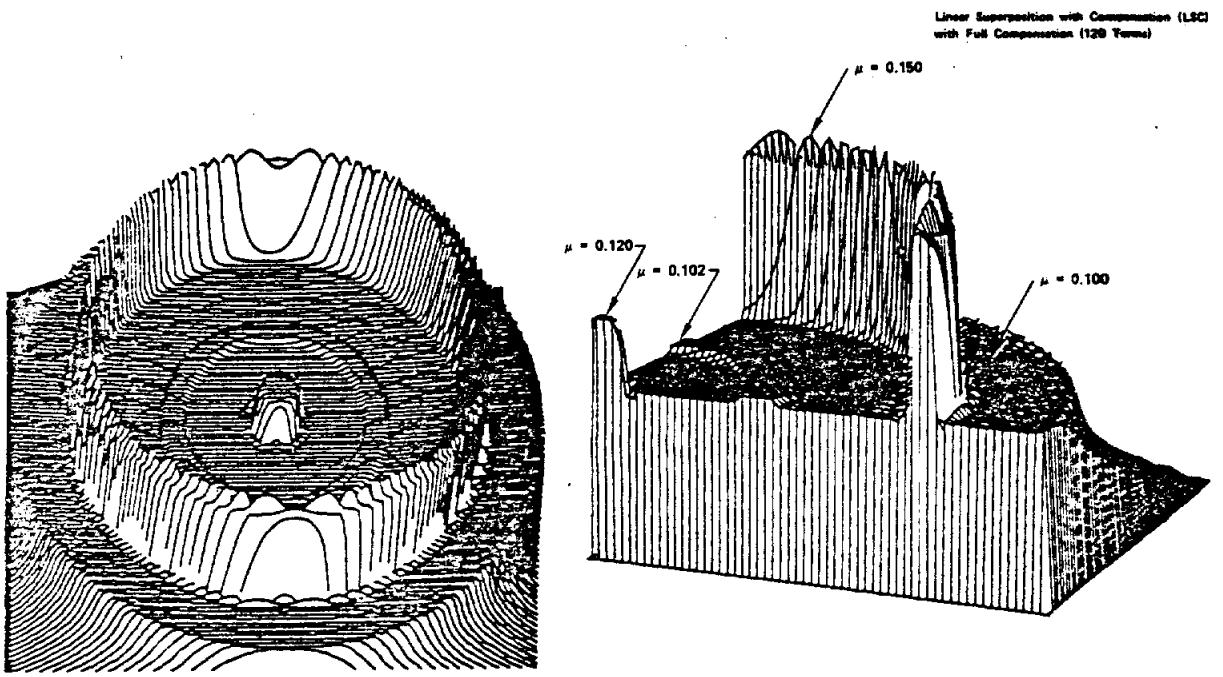

FULL 120 x 120 MATRIX

A QUADRANT OF 120 x 120

Figure 7.

Fig. 5, 6, 7. Gradual recovery of actual image by deconvolutions. Figs. 5 and 6 are with incomplete transfer function (truncated), as indicated, while Fig. 7 is with complete transfer function, i.e., ±120 terms. It is important to note that incomplete transfer function produces uneven background which could result in ambiguity in image visualization.

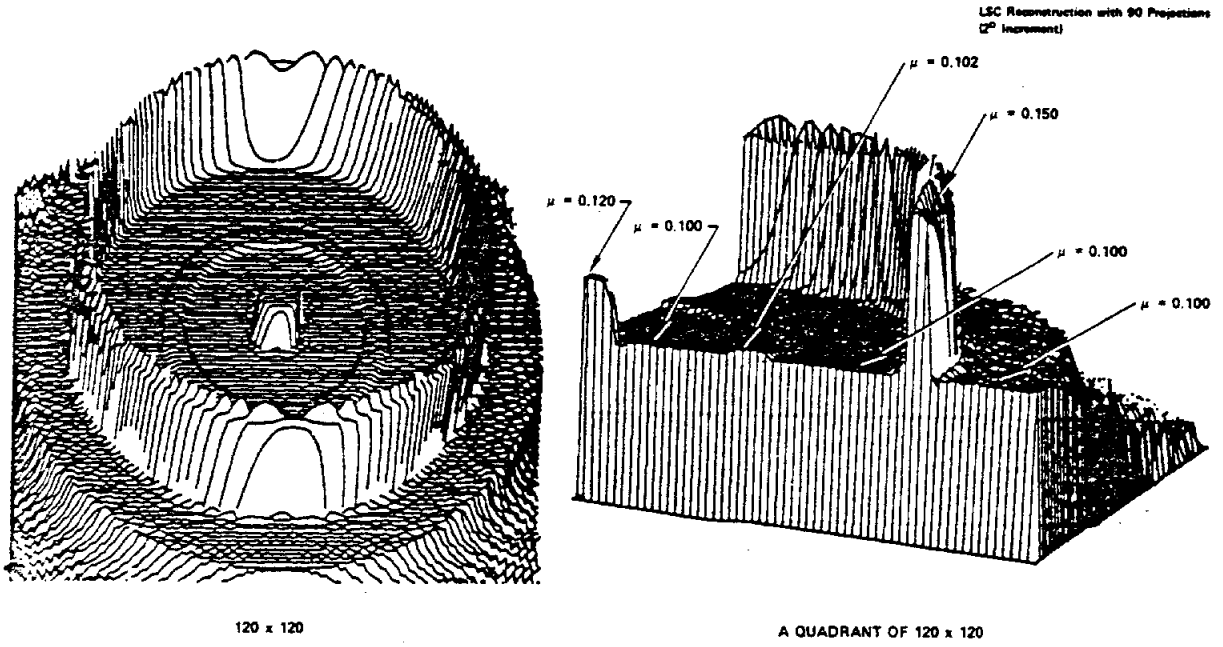

Fig. 8. Same image as Fig. 7, with lower projection data (90 projections).

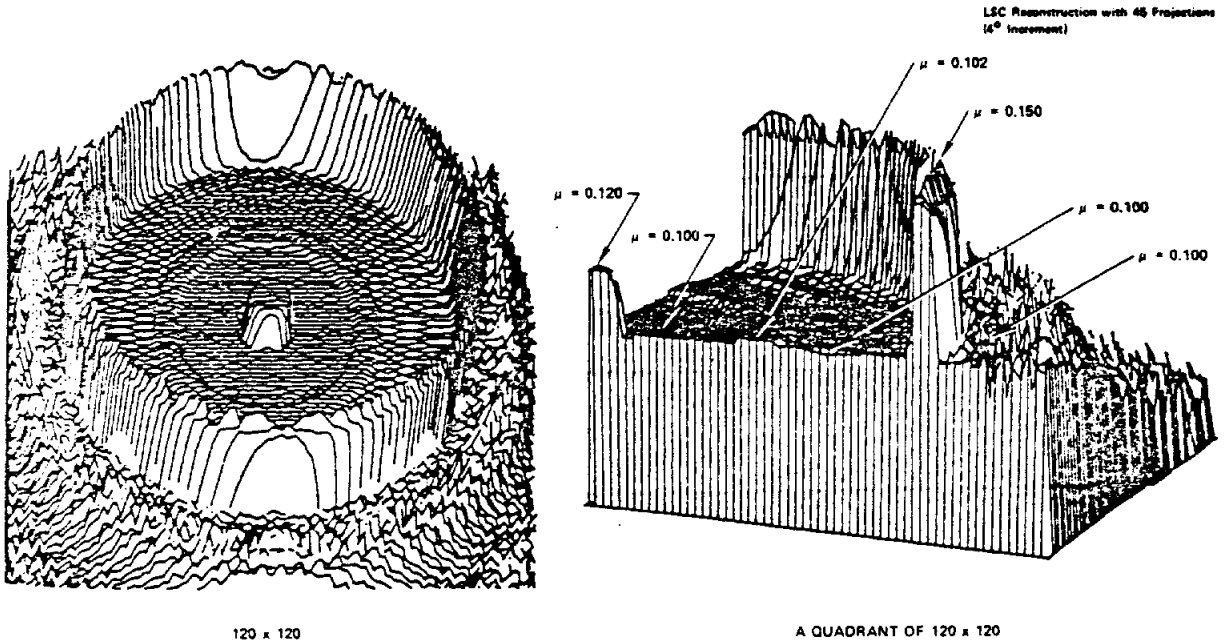

Fig. 9. Same as Fig. 7, with 45 projection data.

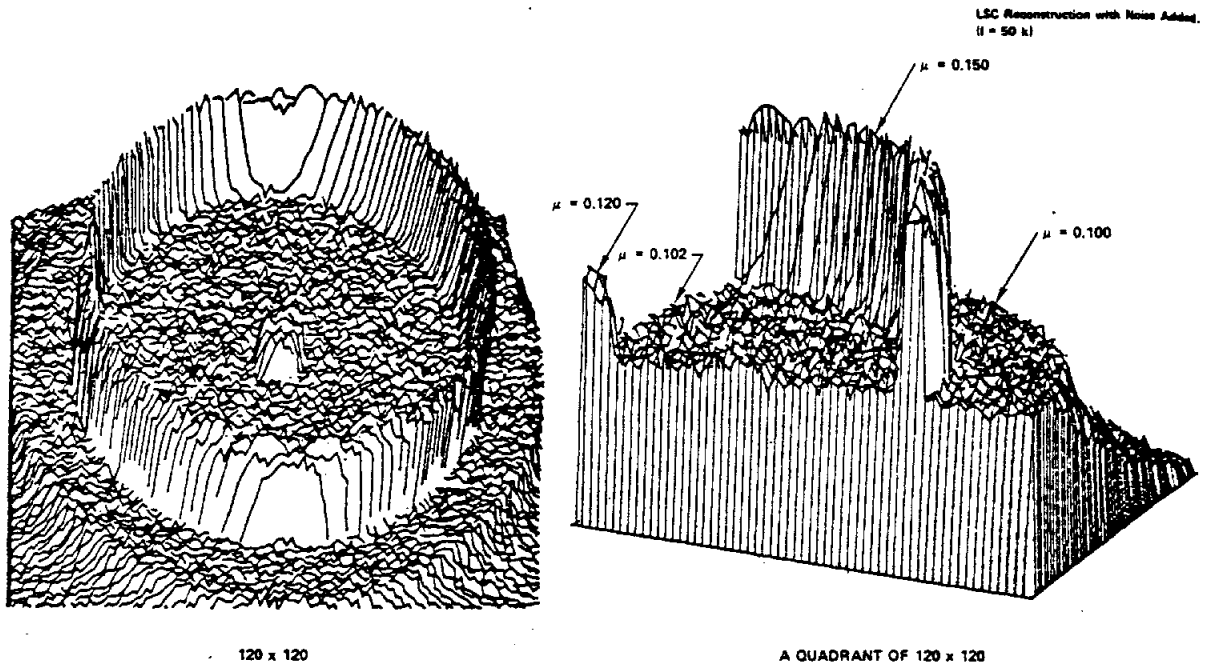

Fig. 10. Same as Fig. 7 with noise added. Each projection data I is assumed 50K.

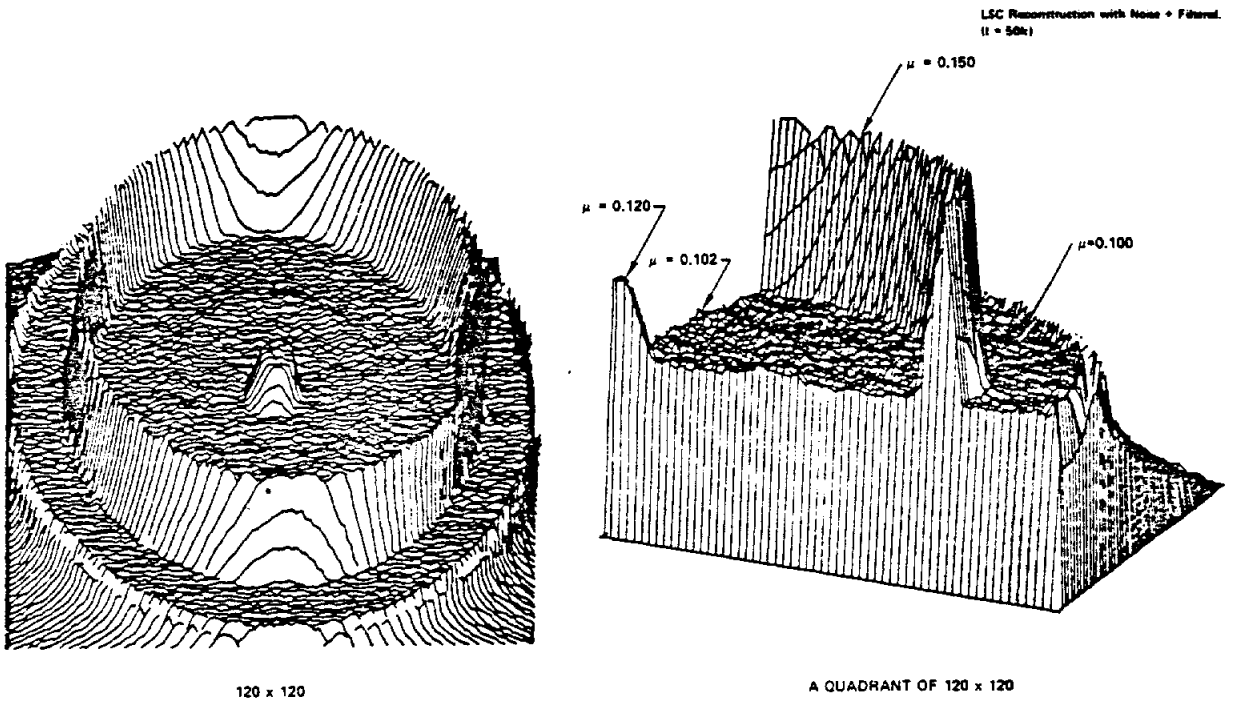

Fig. 11. Same as Fig. 10, with filtering (simple linear interpolation).

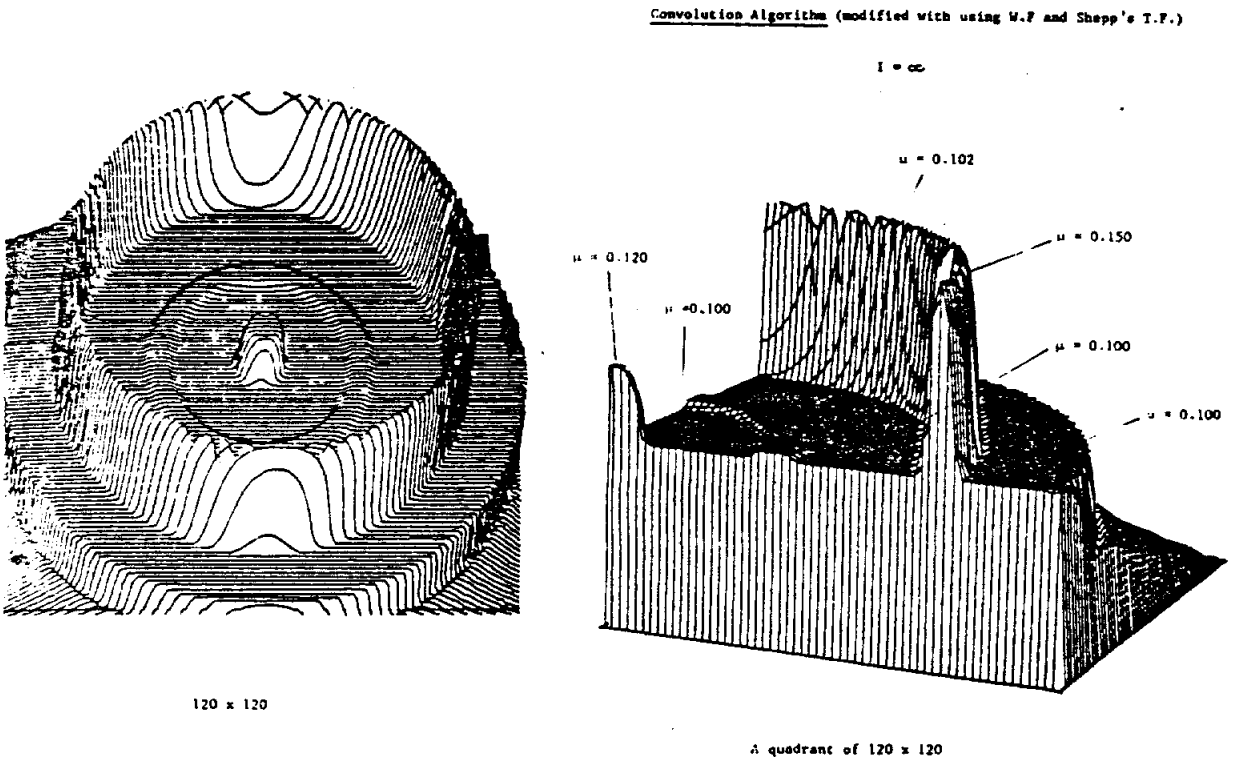

Fig. 12. Image reconstructed with convolution transfer function derived by Shepp and Logan [8].

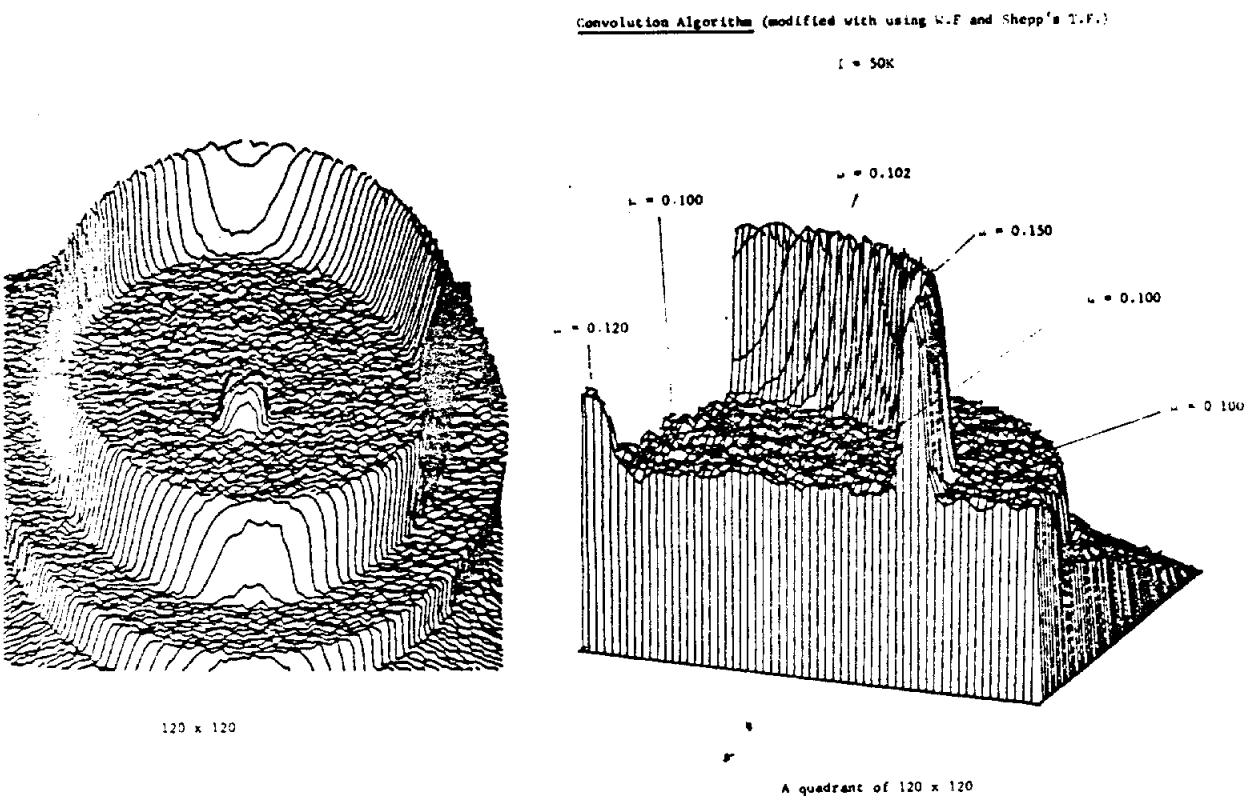

Fig. 13. Same as Fig. 11 (convolution with noise added (I = 50 K).

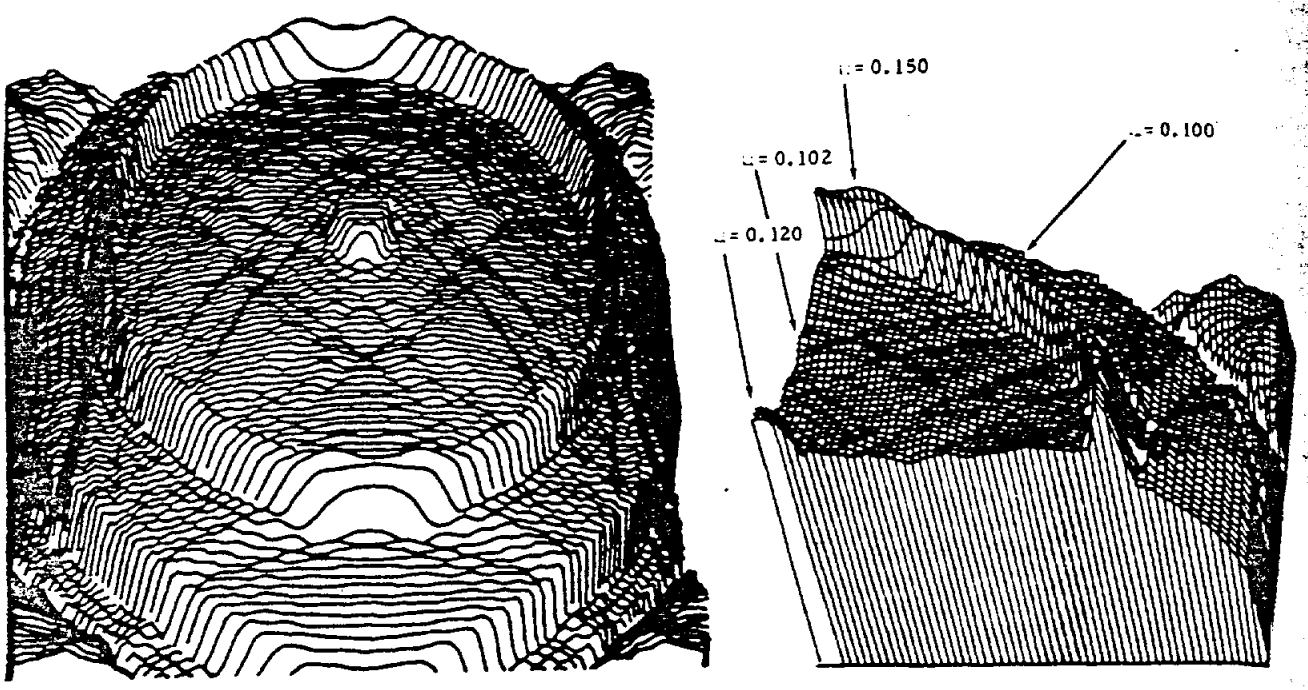

120 x 120 (a) A quadrant of 120 by 120

Fourier Transform Frequency Interpolation

Fourier Bessel Reconstruction

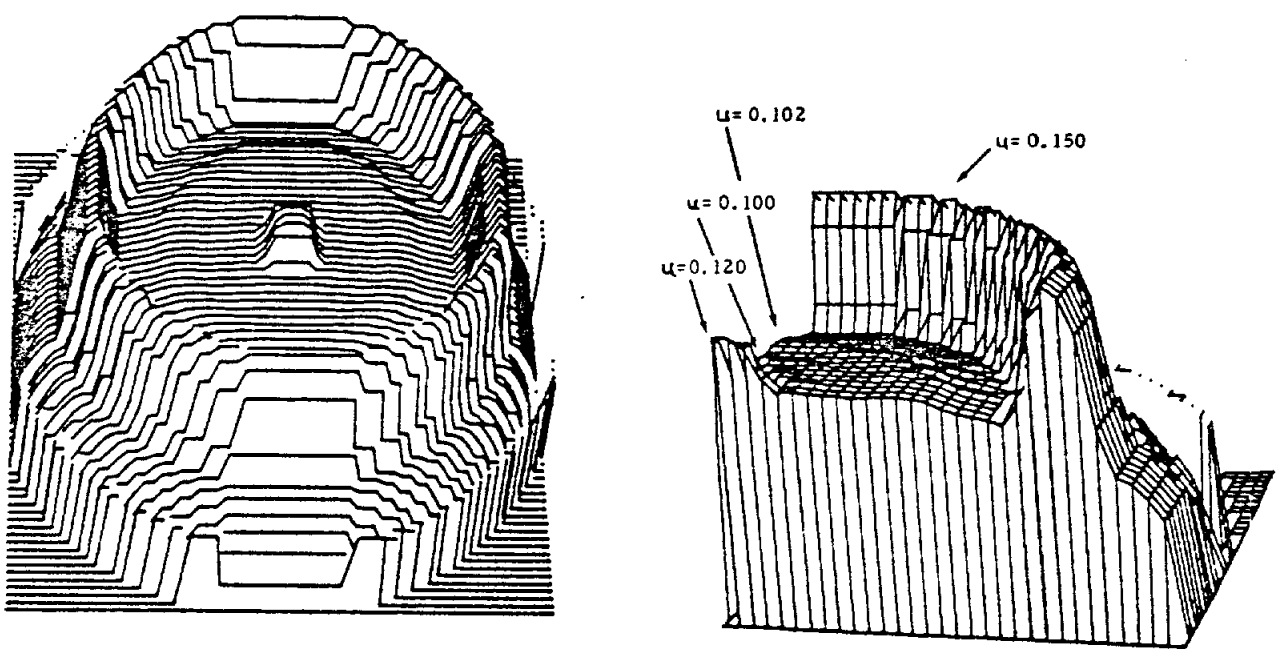

64 x 64 (b) A quadrant of 64 x 64

Fig. 14. Fourier reconstruction (120 projections) without noise (a) Fast Fourier transform with frequency domain interpolation (b) Fourier-Bessel one dimensional Fourier transformation.

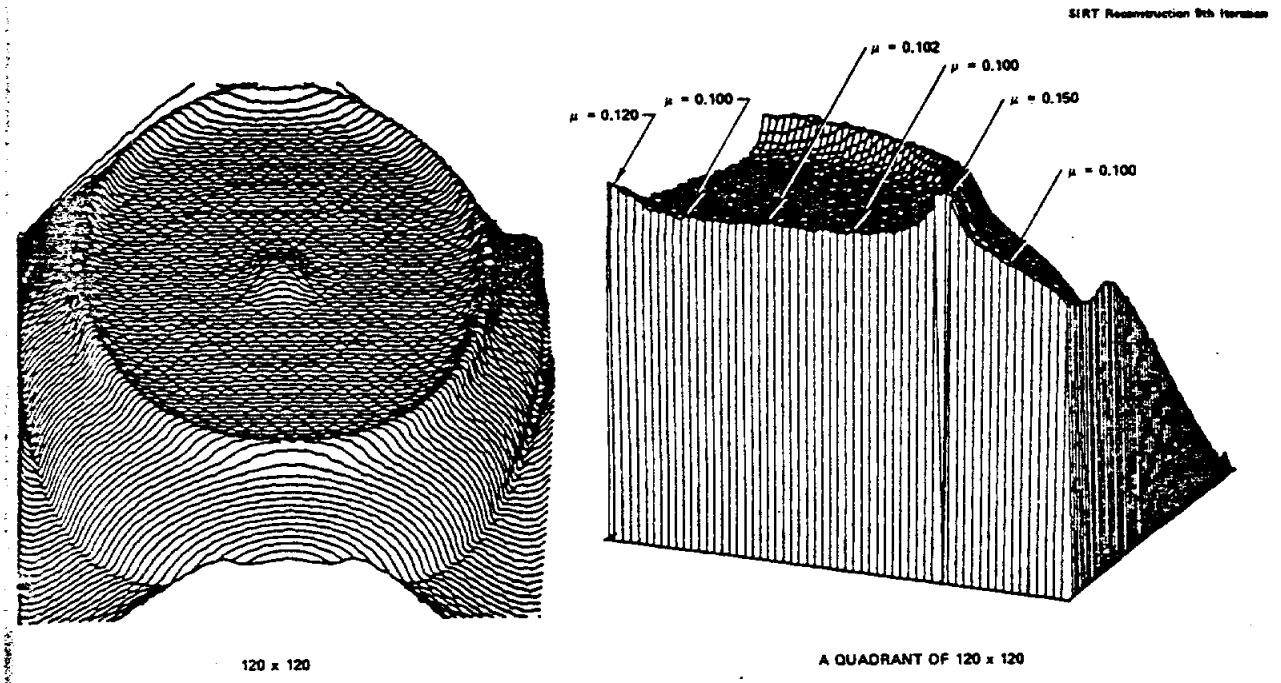

Fig. 15. Reconstruction of same phantom (Fig. 7) with weighted SIRT (9th iterations).

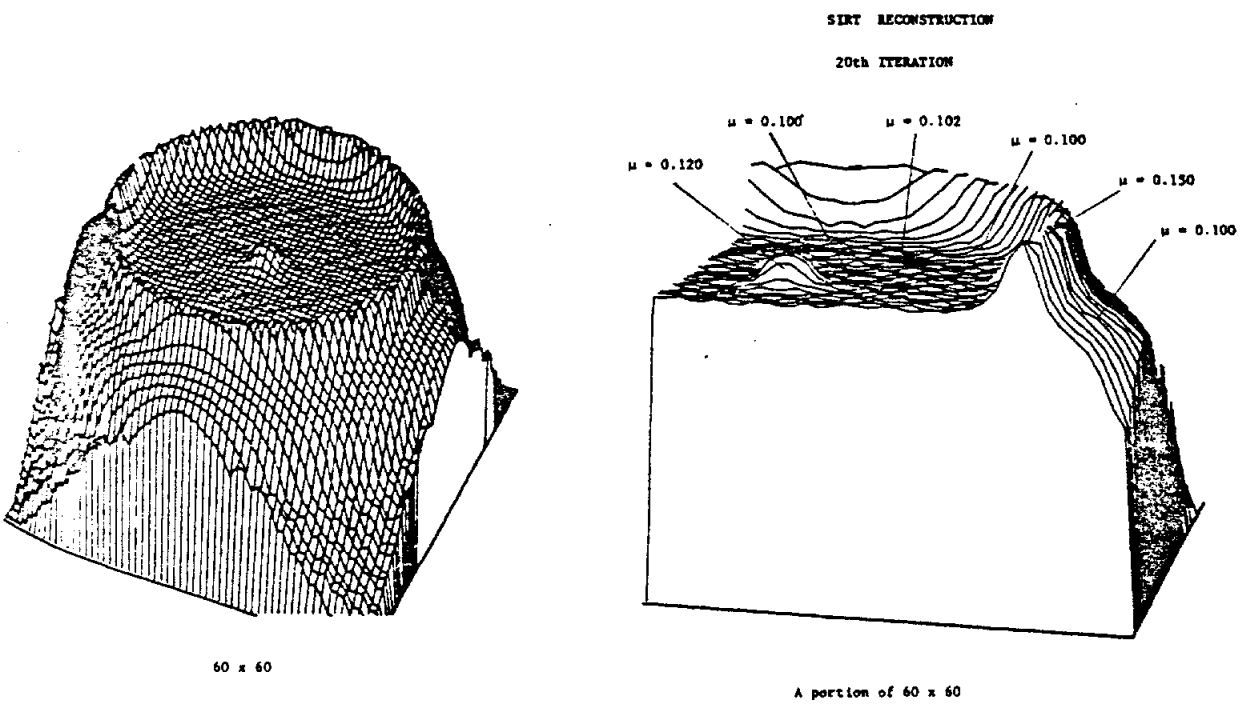

Fig. 16. Same as Fig. 15 with 20th iteration (weighted SIRT).

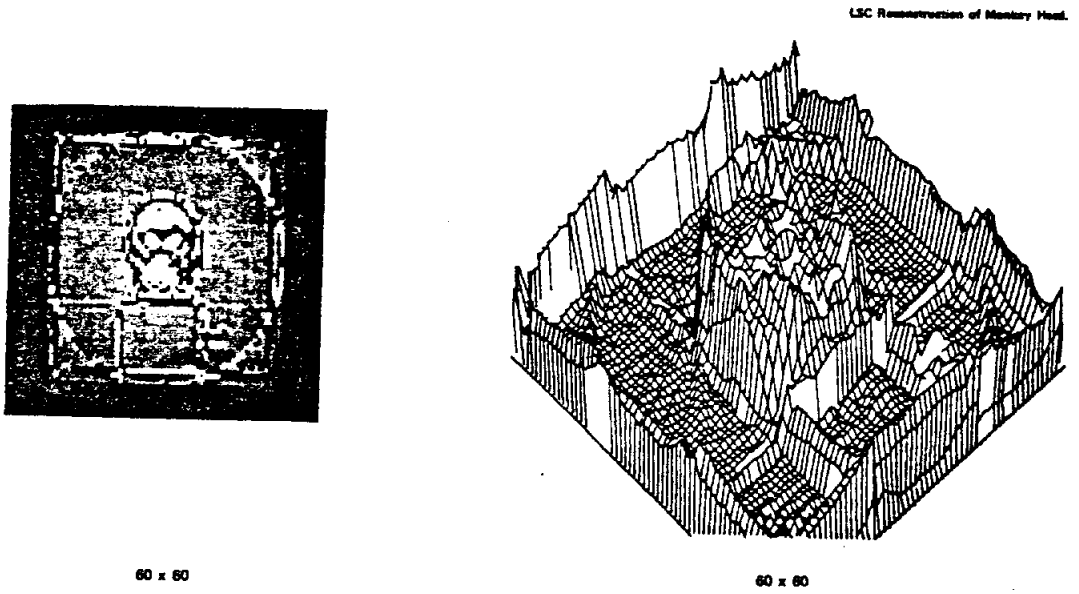

Fig. 17. Cross section image of a monkey head reconstructed with UCLA CTAT scanner using nuclear isotope source (Gd^{153}) and LSC algorithm. The right hand side figure is isometric display of the image shown in the left.